
Cross-Kerr nonlinearity in paraxial fluids of light

Georgios Paraskevopoulos

June 24, 2025

Academic Year 2024 – 2025

Research Unit: Laboratoire Kastler Brossel

Team: Quantum Optics

Supervisor: Q. Glorieux

Abstract

Quantum fluids of light reproduce the hydrodynamics of ultracold Bose–Einstein condensates in an optical setting. In this internship, I contributed to a two-colour ^{85}Rb vapour experiment, realigning the dual-laser optics and automating off-axis interferometric imaging to probe self- and cross-Kerr nonlinearities. The upgraded setup yielded a self-Kerr index $|n_2 I| \approx 10^{-5}$ and a full map of the cross-Kerr index $|n_{12} I| \approx 10^{-6}$, revealing frequency windows where inter-component interactions switch signs.

Keywords: Quantum fluids of light, nonlinear optics, self-Kerr nonlinearity, cross-Kerr nonlinearity, binary mixtures of light

Contents

1	Introduction	3
2	Theoretical description	3
2.1	Nonlinear optics	3
2.2	Nonlinear Schrödinger and Gross-Pitaevskii equations (NLSE & GPE)	5
2.3	Hot atomic vapours	6
3	Experimental methods	7
3.1	Experimental setup	7
3.2	Phase measurement: Off-axis interferometry	8
4	Data acquisition and analysis	10
5	Results	11
6	Conclusion	14
	Références	15

1 Introduction

The internship took place at the Laboratoire Kastler Brossel over the course of over a month, from the 22nd of April to the 13th of June, within the Quantum Fluids of Light research team. In a broad sense, the team studies the quantum fluid effects of light. Normally, light does not have mass, and cannot interact with itself, meaning it is impossible to observe fluid-like effects since they require inter-component interactions.

However, curiously, it is possible to engineer a two-dimensional fluid of light in a nonlinear medium. The medium gives photons an effective mass, and acts as a mediator of photon-photon interactions.

This approach gives a unique perspective into the study of quantum fluids; using the toolkits and techniques of optics to our advantage, one can probe into the physics of quantum hydrodynamic systems (BEC, superfluidity) while circumnavigating the difficulties of experimentally realising quantum fluids through ultracold atomic gases.

Initially, I spent a week reading up on the literature of this exciting domain to get up to speed with the quantum fluids of light community. Of much help was the team's recently published review on paraxial fluids of light¹. It gives a comprehensive overview of the team's work, as well as other research groups. Another great resource was T. Aladjidi's thesis, *Full optical control of quantum fluids of light in hot atomic vapors*².

After discussing with the internship's supervisor, Quentin Glorieux, it was decided that I would be focusing on the cross-Kerr nonlinearity effect. In a binary light mixture, both fluids of light interact with each other, altering their refractive index and overall Kerr nonlinearity through intra-component interactions. Understanding this effect is crucial in binary fluids of light settings, where the Kerr nonlinearity of each respective fluid determines the miscibility regime of the mixture. Binary mixtures of light have already been realised within the research team, mainly by Clara Piekarski, however, many questions regarding the miscibility regimes and coarsening dynamics remain^{3,4}.

Although the experimental setup used for the nonlinearity measurements was already set up, it was far from finished. Much of the internship was spent on modifying the experimental setup by adding optical elements (convergent lenses for 4f-systems, neutral density filters, etc.), removing certain elements that were deemed unnecessary, working on the alignment of the optical paths, and choosing an ideal rubidium vapour cell. This was done with the aid of PhD student Simon Lepleux, who was of great help throughout the internship.

A significant amount of time was also dedicated towards the development of a Python script to interface one of the cameras with both lasers and a computer. The use for this was twofold; first, it significantly eased the optical alignment of the light beams since it allowed to not only obtain live images from the camera, but also image the Fourier plane in real time. Second, it allowed to perform the necessary data treatment to obtain the phase of the fluid beam over many image frames within a short window of time.

2 Theoretical description

2.1 Nonlinear optics

Optical phenomena are considered nonlinear when the response of a medium to an applied electric field is dependent on higher order powers of the electric field. In order to describe this nonlinearity, it is necessary to delve into the polarisation $\mathbf{P}(t)$ of a medium, which is none other than the dipole moment per unit of volume.

In «standard» linear optics, the polarisation of a dielectric medium induced by an incident electric field follows a simple linear relationship; $\mathbf{P}(t) = \epsilon_0 \chi^{(1)} \mathbf{E}(t)$, where $\chi^{(1)}$ is the so-called linear susceptibility

and ε_0 is the vacuum permittivity.

On the other hand, in nonlinear optics, the polarisation is expanded into a series of increasing orders of power of the applied electric field,

$$\mathbf{P} = \varepsilon_0 [\hat{\chi}^{(1)} \cdot \mathbf{E} + \hat{\chi}^{(2)} : \mathbf{E}\mathbf{E} + \hat{\chi}^{(3)} : \mathbf{E}\mathbf{E}\mathbf{E} + \dots]. \quad (1)$$

In all generality, $\hat{\chi}^{(n)}$ is the n -th order susceptibility, and a tensor of rank $n + 1$. The dot notation in the above equation denotes tensor products.

Keeping track of all tensor elements of susceptibility can quickly become cumbersome. Already at the third order of susceptibility, one must take into account 81 elements. Thankfully, a few considerations in the symmetry of a system can alleviate this problem.

Indeed, in a medium with central symmetry such as a vapour, all susceptibilities of even order vanish⁵. One can see this explicitly with the second order susceptibility. Consider for example the following polarisation, containing only second order dependence, $\mathbf{P}(t) = \varepsilon_0 \chi^{(2)} \mathbf{E}^2(t)$. Changing the sign of the electric field, the sign of the polarisation must also change, since by assumption the medium is centrosymmetric (in other words it possesses an inversion symmetry). The previous expression thus becomes $-\mathbf{P}(t) = \varepsilon_0 \chi^{(2)} [-\mathbf{E}(t)]^2 = \varepsilon_0 \chi^{(2)} \mathbf{E}(t)^2$. Since $\mathbf{P}(t) = -\mathbf{P}(t)$, it follows that $\mathbf{P}(t) = 0$ and thus $\chi^{(2)} = 0$.

Furthermore, assuming an isotropic and linearly polarised electric field, which is indeed valid in our case, all susceptibilities simplify into scalar values. Taking into account only values up to the third order, we obtain the following simplified expression for the polarisation of the medium:

$$P(t) = \varepsilon_0 \chi^{(1)} E(t) + \varepsilon_0 \chi^{(3)} E^3(t). \quad (2)$$

The incident electric field is assumed to be monochromatic; $E(t) = \frac{1}{2} E_0 e^{i\omega t} + \text{c.c.}$. Cubing this expression gives us $E^3(t) = \frac{1}{8} (3E_0 |E_0|^2 e^{-i\omega t} + E_0^3 e^{-3i\omega t} + \text{c.c.})$. Putting these two expressions of the electric field into equation 2, one obtains the following induced polarisation:

$$P(t) = \frac{P_0}{2} e^{-i\omega t} + \frac{P_1}{2} e^{-3i\omega t} + \text{c.c.} \quad (3)$$

with $P_0 = \varepsilon_0 \chi^{(1)}(\omega) E_0 + \frac{3}{4} \varepsilon_0 \chi^{(3)}(\omega) |E_0|^2 E_0$, and $P_1 = \frac{1}{4} \varepsilon_0 \chi^{(3)}(3\omega) E_0^3$. The value in the parenthesis of each susceptibility denotes the frequency at which the respective term oscillates.

The contribution of the term P_1 being negligible near resonance, equation 3 is further simplified into

$$P(t) = \varepsilon_0 \left(\frac{1}{2} \chi^{(1)}(\omega) + \frac{3}{8} \chi^{(3)}(\omega) |E_0|^2 \right) E_0 e^{-i\omega t} + \text{c.c.} \quad (4)$$

The total susceptibility can then be defined as $\chi = \chi^{(1)} + \frac{3}{4} \chi^{(3)} |E_0|^2$. This expression allow us to finally proceed with deriving the refractive index expression. Skipping over a few tedious but simple steps, one arrives at the following equation for the refractive index:

$$n(\mathbf{r}) = n_0 + \delta n_0(\mathbf{r}) + n_2 I, \quad (5)$$

where n_0 is the ordinary linear refractive index, $\delta n_0(\mathbf{r})$ describes local variations, and $n_2 I$ is the nonlinear contribution to the refractive index, proportional to the intensity of the light.

This equation is paramount for the rest of this paper. The nonlinear refractive index $n_2 = \frac{3\chi^{(3)}}{4\varepsilon_0 n_0^2 c}$, which is directly proportional to the third-order susceptibility, is also known as self-Kerr nonlinearity, and is at the basis of the nonlinear optical behaviour that we see manifested within the medium.

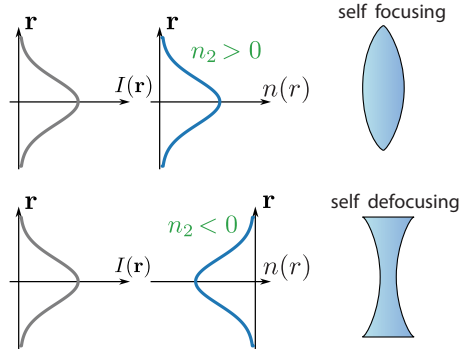


Figure 1: Depiction of the analogy between convergent and divergent lenses in the case of a light beam with a gaussian intensity profile traversing a nonlinear medium.²

The most crucial property that arises from self-Kerr nonlinearity is the so-called self-focusing and self-defocusing regimes. Imagine a light beam with a gaussian intensity profile. For a positive n_2 , the centre of the light beam will experience a higher refractive index compared to its outskirts, similarly to a convergent lens, and thus self-focus. For a negative n_2 , this will lead to self-defocusing, analogously to a divergent lens. This principle is qualitatively demonstrated in figure 1.

In a binary fluid of light mixture, interactions between both fluids give rise to another effect, the so-called cross-Kerr nonlinearity. This added effect contributes to the total refractive index, altering the self-(de)focusing regime. The cross-Kerr nonlinear index is denoted as n_{12} .

2.2 Nonlinear Schrödinger and Gross-Pitaevskii equations (NLSE & GPE)

The NLSE describes the evolution of the electric field envelope as it propagates through a nonlinear medium. The full derivation of the NLSE will not be detailed here, but a few crucial assumptions for its validity are outlined.

The NLSE is derived from the following Maxwell's equation describing the propagation of an electric field through a nonlinear material,⁶

$$\nabla^2 \mathbf{E} - \frac{1}{c^2} \frac{\partial^2 \mathbf{E}}{\partial t^2} = \frac{1}{\epsilon_0 c^2} \frac{\partial^2 \mathbf{P}}{\partial t^2}. \quad (6)$$

An important assumption is that the envelope \mathcal{E} of the electric field $E = \mathcal{E} e^{ik_0 z}$ varies slowly comparatively to the wavenumber k_0 . This assumption naturally leads to the paraxial approximation.

Eventually, the 2D+1 NLSE is obtained:

$$i \frac{\partial \mathcal{E}}{\partial z} = -\frac{1}{2k_0} \nabla_{\perp}^2 \mathcal{E} - i \frac{\alpha}{2} \mathcal{E} - k_0 \frac{\delta n_0(\mathbf{r})}{n_0} \mathcal{E} - k_0 \frac{n_2 I}{n_0} \mathcal{E}, \quad (7)$$

where z is the axis of propagation, and \perp denotes the transverse plane (x, y) .

The whole principle of quantum fluids of light relies on the fact that the NLSE is mathematically analogous to the Gross-Pitaevskii equation, describing the temporal evolution of the macroscopic wavefunction ψ of a dilute Bose gas,

$$i \hbar \frac{\partial \psi}{\partial t} = \left(-\frac{\hbar^2}{2m} \nabla^2 - i \frac{\gamma}{2} + V(\mathbf{r}) + g |\psi|^2 \right) \psi. \quad (8)$$

One can quite easily see the similarities of these two equations. The first term corresponds to the kinetic energy. The second term describes linear loss. The third term is the potential energy, which in the NLSE

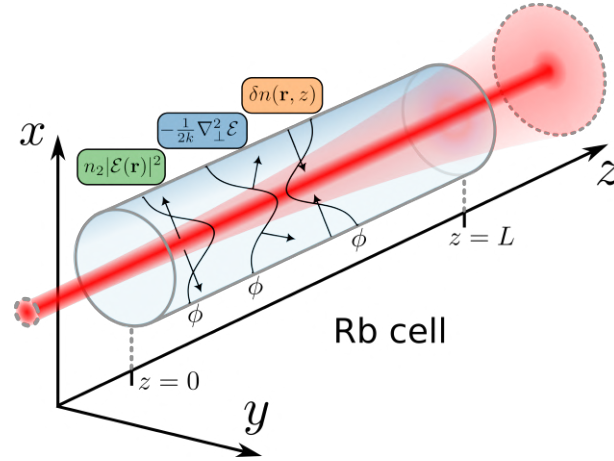


Figure 2: Three dimensional diagram of a fluid beam in the self-defocusing regime. As it passes through the vapour cell, the fluid gradually increases in size. The dynamics of the fluid are governed by the self-Kerr interaction $n_2|\mathcal{E}(\mathbf{r})|^2$, kinetic energy or diffraction $-\frac{1}{2k}\nabla_{\perp}^2\mathcal{E}$, as well as a potential $\delta n(\mathbf{r}, z)$.²

case can be engineered by locally modifying the linear refractive index. Finally, the last term corresponds to a nonlinear self-interaction energy.

An important difference between the two equations, besides the differing dimensions of their quantities, is the fact that while the GPE defines a temporal evolution, the NLSE is describing the evolution along a propagating spatial axis. In essence, the spatial axis z is an effective time dimension, while the spatial dynamics of the fluid of light happen within the transverse plane (x, y) . A nonlinear material of length L will thus have an effective time evolution of L/c .

2.3 Hot atomic vapours

Much of the theoretical framework regarding fluids of light has been laid out in the previous sections. A key consideration that remains is the choice of nonlinear medium.

While there exists a variety of possible nonlinear media that could be used for the experimental realisation of fluids of light, such as photorefractive crystals, or thermo-optic media, the QFL team at LKB is focused primarily on hot atomic vapours of rubidium. Atomic gases exhibit strong nonlinearity when excited by a near resonant laser field.

I will not delve into the details of the theoretical considerations, choosing only to demonstrate the practical necessities for the experiments conducted. There are essentially only 3 experimental parameters that one can manipulate to modify the Kerr nonlinearity in an atomic vapour platform.

Firstly, in an atomic vapour cell the density of the atomic cloud is dependent on its temperature. An empirical equation for the gas pressure (in units of Torr) inside the cell is given⁷,

$$\log_{10} P_{\text{Rb}} = 15.88 - \frac{4529}{T} + 0.000586 T - 2.99 \log_{10} T, \quad (9)$$

valid for $T \geq 312$. Using the ideal gas law, it is possible to link the pressure to the atom density in the cell, $N = P_{\text{Rb}}/k_b T$. We thus have direct and easy control over the interaction strength via the temperature.

Secondly, the detuning of the near-resonant laser field provides crucial control over the strength and sign of the third-order susceptibility $\chi^{(3)}$, and thus the nonlinear refractive index n_2 . While the analytic expression of $\chi^{(3)}$ is more complicated, at large detuning it follows a simple law;

$$\Re(\chi^{(3)}) \propto \frac{N}{\Delta^3}, \quad (10)$$

where N is the atomic density, controlled by the temperature, and Δ is the detuning from the resonant frequency of the transition we've selected.

Depending on the sign of the detuning, the system will exhibit either self-focusing ($\Delta > 0$, equivalent to attractive inter-photon interactions), or self-defocusing ($\Delta < 0$, equivalent to repulsive inter-photon interactions).

It should be noted that the expression 10 is only valid for large detuning. One could incorrectly assume that they could dramatically increase the nonlinearity by reducing the detuning Δ as much as possible, but it should not be forgotten that there is linear absorption at play for small detuning.

The detuning Δ must thus be carefully chosen; there is a trade-off between nonlinearity and linear absorption that must be considered.

Finally, the nonlinear effects can be enhanced by increasing the fluid beam intensity, since the nonlinear contribution to the total refractive index is $n_2 I$.

There is a significant caveat to this, mainly due to the fact that at higher intensity, higher order susceptibilities, such as the fifth-order susceptibility $\chi^{(5)}$ which has an opposite sign to $\chi^{(3)}$, become prominent, reducing the nonlinear effects. This is accounted for by what is called the saturation intensity. A more accurate expression for the total refractive index would therefore be

$$n = n_0 + \frac{n_2}{n_0} \frac{I}{1 + I/I_{sat}(\Delta)}, \quad (11)$$

with the saturation intensity $I_{sat}(\Delta) = I_{sat}(0) \left(1 + \frac{\Delta^2}{\Gamma^2}\right)$, where $I_{sat}(0) = \frac{\pi \hbar \omega_0 \Gamma}{3\lambda^3}$ and Γ are the saturation intensity at resonance, and the linewidth of the atomic transition in question.

3 Experimental methods

The standard method for the characterisation of nonlinear optical properties of materials is the so-called z-scan technique⁸. However, in our case, off-axis interferometry is employed, which doesn't require scanning the nonlinear material over any range. Instead, a Mach-Zehnder type interferometer is used, with the reference and fluid beams having a relative angle between them. Following the phase retrieval procedure described in subsection 3.2, it is possible to gain access to the self-Kerr and cross-Kerr nonlinearity through the self-phase modulation.

Though self-Kerr nonlinearity has already been detailed in subsection 2.1, the main goal during this internship was to study the effects of cross-Kerr nonlinearity between two fluid beams, meaning the nonlinearity that one fluid beam attributes to the other, as they propagate through the nonlinear medium. To this end, an experimental setup was needed where two separate laser beams can be independently controlled, both in intensity and frequency in order to study the effects of cross-Kerr nonlinearity, all while having control over these two parameters.

3.1 Experimental setup

The experimental setup essentially consists of two independent lasers, both of which traverse the rubidium vapour cell, as well as two Mach-Zehnder interferometers⁹. In the following paragraphs, the path of one of the laser beams is detailed to better understand its functionality.

The linearly polarised laser beam initially passes through a half-wave plate and a polarising beam splitter, giving crucial control over the fraction of light going into the reference and fluid beams.

Following the fluid beam, it first passes through the rubidium vapour cell, where it spatially overlaps with the other fluid beam. This is crucial to study the effects of cross-Kerr nonlinearity. A polarising beam

splitter then separates the two fluid beams issued from each laser. A simple beam splitter then recombines the reference and fluid beams to be imaged onto the camera.

The half-wave plate preceding the beam splitter allows for the manipulation of the fluid beam polarisation. It is essential to ensure that both reference and fluid beams are polarised in the same direction when recombined; otherwise, the interference fringes will have a severely low contrast, or even be non-existent in the case where the beams are cross-linearly polarised.

Figure 3 provides a simplified schematic of the experimental setup. Missing from the diagram are several key optical elements:

First and foremost, a 4f telescope system is included in both reference and fluid branches of the setup, albeit for different reasons.

In the reference branch, two convergent lenses with carefully selected focal points f_1 and f_2 are selected, such that the reference is magnified by a factor of $f_2/f_1 > 1$.

Concerning the fluid beam, a 4f-system is used to image the fluid beam directly at the exit of the rubidium cell, thus limiting diffraction due to free space propagation.

Finally, neutral density filters are placed on the optical path of both beams, so as not to saturate and damage the camera sensor.

Regarding the choice of the rubidium vapour cell, it was decided beforehand that a single isotope vapour would be used, as it has an energetic landscape that is much simpler than that of a naturally occurring rubidium gas, which contains two isotopes. This significantly simplified detuning considerations, as we had to take into account only two transitions of the ^{85}Rb D1 line; $5^2S_{1/2}, F = 2, 3 \rightarrow 5^2P_{1/2}$. The hyperfine structure of the excited state is deemed irrelevant since it is undetectable due to thermal Doppler broadening.

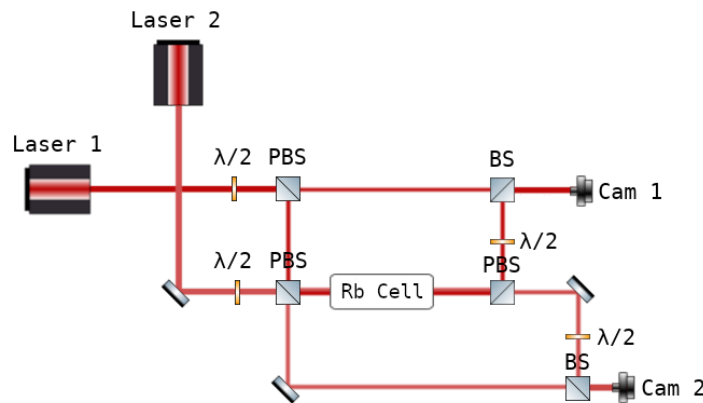


Figure 3: Simplified schematic diagram of the experimental setup. Different shades of red are used to differentiate the beams issued from lasers 1 and 2. Half of the light intensity which is lost through the beam splitters, as well as the 4f-systems and neutral density filters are not depicted to avoid a cluttered diagram.

3.2 Phase measurement: Off-axis interferometry

Unlike ultracold atomic gases, the phase of fluids of light is relatively easy to extract through interferometric techniques. In our case, off-axis interferometry is used to measure the self-phase modulation of the fluid beam. This gives paraxial fluids of light a considerable advantage over ultracold atomic gases, as a well adjusted setup allows for rapid phase retrieval of up to several dozen Hz .

Consider a fluid and reference beam, E_f and E_r respectively, superposed with a certain angle. \mathbf{k}_\perp denotes the transverse wavevector of the reference beam with respect to the signal, which is null if the angle between the two beams is also null. This configuration creates interference patterns, which are imaged on the camera.

The signal imaged on the camera will be proportional to the intensity of both fluid and reference beam envelopes,

$$I_{\text{cam}}(\mathbf{r}_\perp) \propto |E_s(\mathbf{r}_\perp)e^{i\phi(\mathbf{r}_\perp)} + E_r(\mathbf{r}_\perp)e^{i\mathbf{k}'_\perp \mathbf{r}_\perp}|^2 = I_s(\mathbf{r}_\perp) + I_r(\mathbf{r}_\perp) + \underbrace{E_s^* E_r e^{-i(\phi - \mathbf{k}'_\perp \mathbf{r}_\perp)} + E_s E_r^* e^{i(\phi - \mathbf{k}'_\perp \mathbf{r}_\perp)}}_{\text{modulated part}}. \quad (12)$$

The first two terms simply give the intensity of each beam. The interference fringes arise from the underlined modulated part.

In order to retrieve the phase $\phi(\mathbf{r}_\perp)$ of the fluid beam, it is necessary to pass into k -space by means of a Fourier Transform. After filtering the appropriate signal from the Fourier plane, the phase is successfully recovered from the interferogram.

Applying the Fourier Transform on $I_{\text{cam}}(\mathbf{r}_\perp)$, the intensity imaged by the camera in k -space is as follows:

$$\tilde{I}_{\text{cam}}(\mathbf{k}_\perp) = \tilde{I}_s(\mathbf{k}_\perp) + \tilde{I}_r(\mathbf{k}_\perp) + \mathcal{F} [E_s e^{i\phi(\mathbf{r}_\perp)}] (\mathbf{k}_\perp) * \{\tilde{E}_r(\mathbf{k}_\perp - \mathbf{k}'_\perp)\} + \mathcal{F} [E_s e^{-i\phi(\mathbf{r}_\perp)}] (\mathbf{k}_\perp) * \{\tilde{E}_r(\mathbf{k}_\perp + \mathbf{k}'_\perp)\}. \quad (13)$$

It is thus possible to extract the phase from the third or fourth term. These terms manifest in k -space in the form of two sidebands (or satellite peaks), symmetric to the zeroth order central peak.

To further simplify equation 13, care is taken to magnify the reference beam, making it much larger than the fluid beam. The reference beam's Fourier transform is therefore much narrower than the fluid beam's, allowing the approximation $\tilde{E}_r(\mathbf{k}_\perp \pm \mathbf{k}'_\perp) \approx \delta(\mathbf{k}_\perp \pm \mathbf{k}'_\perp)$. The convolution product is therefore a simple shift by \mathbf{k}'_\perp .

Following the above procedure, the intensity is simplified;

$$\tilde{I}_{\text{cam}}(\mathbf{k}_\perp) \approx \tilde{I}_s(\mathbf{k}_\perp) + \tilde{I}_r(\mathbf{k}_\perp) + \underbrace{\mathcal{F} [E_s e^{i\phi(\mathbf{r}_\perp)}] (\mathbf{k}_\perp + \mathbf{k}'_\perp) + \mathcal{F} [E_s^* e^{-i\phi(\mathbf{r}_\perp)}] (\mathbf{k}_\perp - \mathbf{k}'_\perp)}_{\text{modulated part (sidebands)}}. \quad (14)$$

The next step of the phase measurement procedure is to spatially filter the image in the Fourier plane, leaving only one of the sidebands. This removes the first two terms, which are contained in the zeroth order peak, leaving only one term from the modulated part of equation 14.

Let $\tilde{T}(\mathbf{k}_\perp)$ be the band-pass filter through which one of the satellite peaks is selected. The filtered intensity is thus $\mathcal{F} [E_s^* e^{\pm i\phi(\mathbf{r}_\perp)}] (\mathbf{k}_\perp \pm \mathbf{k}'_\perp) * \tilde{T}(\mathbf{k}_\perp)$.

Finally, by applying the inverse Fourier transform on the filtered sideband, and by shifting the signal by $\pm \mathbf{k}'_\perp$ (the sign depends on which sideband was selected, the shifting rolls the filtered signal to the centre of the Fourier plane), the following signal is retrieved:

$$E_s e^{\pm i\phi(\mathbf{r}_\perp)} * \mathcal{F}^{-1} [\tilde{T}] (\mathbf{r}_\perp). \quad (15)$$

The phase is consequently retrievable through the argument of expression 15. Of course, the density (or intensity) of the fluid beam is also accessible through the magnitude of the aforementioned expression.

It should be noted that if the band-pass filter used is circular in form, its inverse Fourier transform $\mathcal{F}^{-1} [\tilde{T}] (\mathbf{r}_\perp)$ gives rise to an Airy disc. To limit the deformation of the recovered field, it is advisable to maximise the radius of the circular filter. This fixes the ideal location of the sidebands in the Fourier

plane to the centre of its quadrants, allowing for the maximal radius of the circular filter, all while filtering out the zeroth order signal.

Figure 4 provides a concise and helpful visual aid to understand the phase retrieval process.

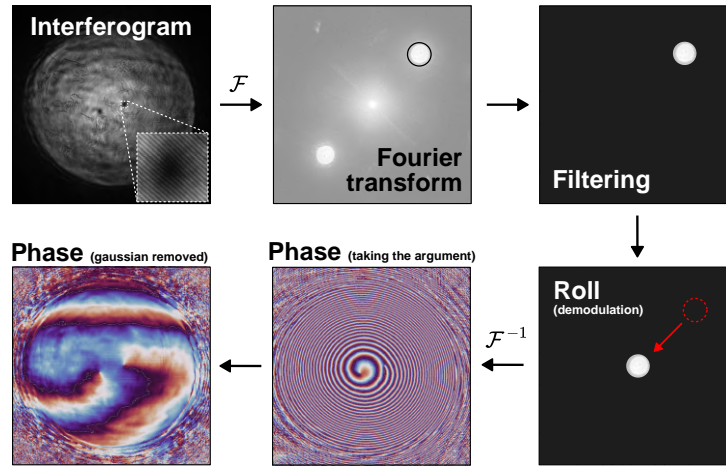


Figure 4: Phase retrieval process. After applying the Fourier transform on the interferogram, one of the sidebands is selected and filtered. The sideband is shifted by \mathbf{k}_\perp , bringing it to the centre of the Fourier plane. The inverse Fourier transform is subsequently applied, and the argument of the signal is taken to retrieve the phase.¹

4 Data acquisition and analysis

Much time during this internship was dedicated to creating an automated interface between the cameras and lasers in order to effectuate the desired measurements at the click of a button.

More specifically, I wrote a Python code interfacing a Point-Grey camera along with the 2 lasers. The code allows for live measurements of the Kerr nonlinearity, using the phase measurement process described in subsection 3.2, all while giving the ability to modulate the frequency of the lasers (through control of the laser temperature) to study the influence of one fluid beam on the other. It also significantly eases the optical alignment of the reference and fluid beam.

After acquiring the nonlinear phase modulation $\phi(\mathbf{r})$ through off-axis interferometry, a cut-off filter is set at 1% of the maximal intensity of the fluid beam in order to filter out noisy data. The phase being modulo 2π , it is unwrapped to reconstruct the complete phase of the fluid beam's wavefront. The azimuthal average of the phase is then calculated in order to acquire the radial phase profile. Nonlinear phase modulation is then calculated by $\phi_{NL} = \phi(r_{max}) - \phi(0)$. Finally, the nonlinear refractive index is retrieved through the expression $\phi_{NL} = k_0 L \Delta n$ ¹⁰, where $k_0 = 2\pi/\lambda$ is the wavenumber of the atomic transition, L is the length of the cell, and $\Delta n = n_2 I$.

An important point of contention with this method is that the percentage at which the cut-off filter is set is quite arbitrary, giving different values of the Kerr nonlinear index for different values of the cut-off point. Unfortunately, it seems that not much is possible to avoid this; as the fluid beam defocuses, the light on the edges of the gaussian profile becomes increasingly spread out and weak in intensity, leading to a noisy phase profile. In any case, the cut-off was fixed at 1%, which seemed to be a good compromise between removing the noisy data and keeping most of the phase profile.

As an example, figures 5 and 6 show the phase profile of a given fluid of light before and after applying the cut-off filter and unwrap.

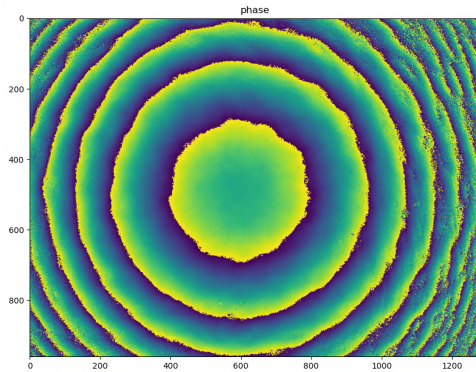


Figure 5: Raw phase profile of a defocusing fluid of light.

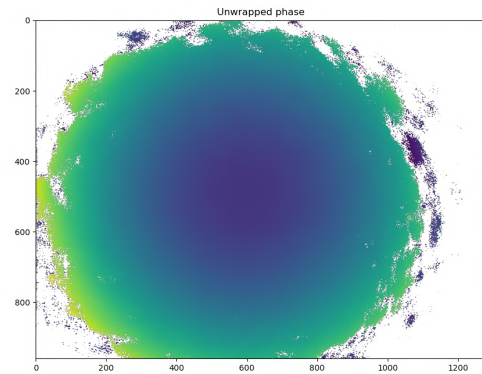


Figure 6: Unwrapped and filtered phase.

Measuring the frequency of the lasers was evidently important for our measurements. Unfortunately, the wavemeter in the lab was quite often unavailable. Instead, the frequencies were measured for various values of the laser temperature; it was found that the relationship between the laser frequency and temperature is almost perfectly linear. After applying a linear regression, this model was used to calculate the frequencies of the laser through its temperature. Figure 7 presents this procedure.

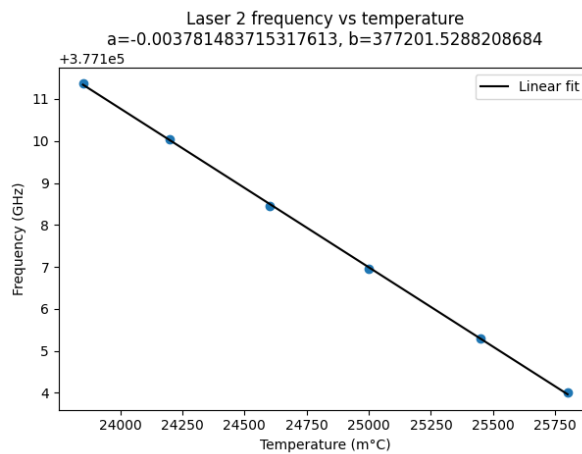


Figure 7: Relationship between the frequency and temperature of laser 2.

5 Results

The main focus was put on the self-defocusing regime, meaning the laser frequency had to be red-detuned ($\Delta < 0$). An 8 cm long ^{85}Rb cell was used. We experimented with a variety of rubidium cells, containing either ^{85}Rb or ^{87}Rb . An ^{85}Rb cell was ultimately chosen because the other cells would imprint weird artifacts on the light when imaged.

The principle of the measurements is the following:

Laser 1 is fixed at a certain red-detuned frequency at which the self-phase modulation seems to be maximal. The self-Kerr refractive index $\Delta n = n_2 I$ is measured via the Point-Grey camera (1). The

second laser beam is then allowed into the system. The nonlinear refractive index of the laser 1 fluid beam is measured for a range of frequencies of the laser 2.

There are mainly two simplified scenarios one can imagine in which the cross-Kerr nonlinearity might be measured.

In the first case, both fluid beams issued from lasers 1 and 2 have the same intensity. Using a power meter, the fluid beams intensity was measured to be around 500 mW. Let's assume $I_1 = I_2 = I_0/2$, with I_1, I_2 the intensity of the fluid beams from lasers 1 and 2, and I_0 the total intensity in the vapour cell. First, a measurement of the self-Kerr nonlinearity of the fluid beam from laser 1 is made, in the absence of laser 2, at intensity $I_1 = I_0/2$, denoted as $\Delta n^{I_0/2} = n_2 I_0/2$. A histogram of the measured $\Delta n^{I_0/2}$ values taken over the course of around 30 seconds is shown in figure 9. Then, adding laser 2 back into the system, another measurement of the nonlinear refractive index is made, this time $\Delta n = (n_{12} + n_2) I_0/2$, where n_{12} is the cross-Kerr nonlinear index. The cross-Kerr nonlinearity can therefore be extracted by $\Delta n - \Delta n^{I_0/2} = n_{12} I_0/2$.

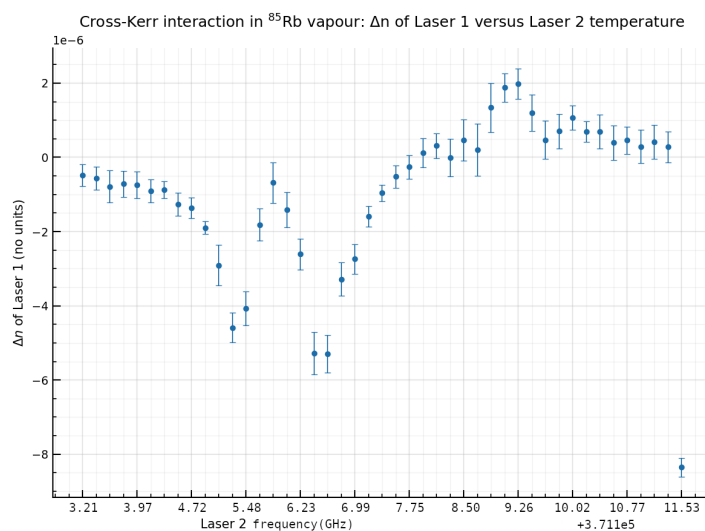


Figure 8: Plot showcasing the cross-Kerr nonlinear index of laser 1 (as explained in the first case of section 5) in function of the frequency of laser 2.

Figure 8 shows the measured cross-Kerr nonlinearity employing the aforementioned method. The cross-Kerr nonlinearity $n_{12}I$ is of the order of 10^{-6} , while the self-Kerr nonlinearity n_2I is typically of the order of 10^{-5} (see figure 9). There seem to be three regions of frequency where the cross-Kerr nonlinearity becomes noticeable. Although no theoretical framework has been made to predict the cross-Kerr nonlinearity, it is theorised that these regions arise in two cases.

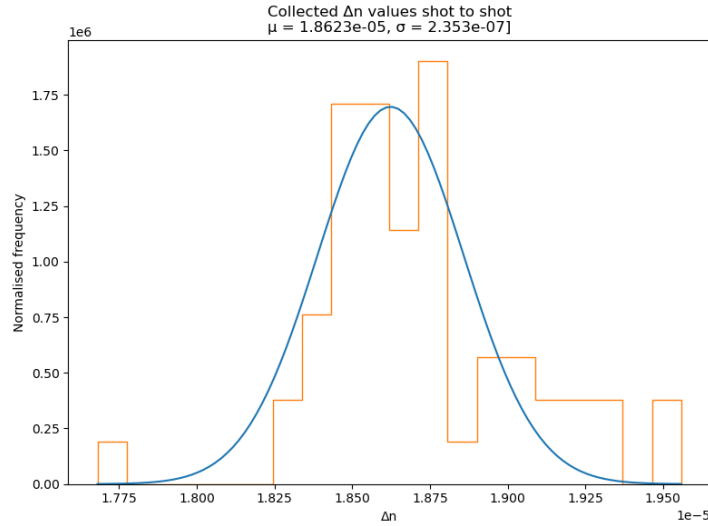


Figure 9: Histogram of the measured self-Kerr nonlinearity values of laser 1, in the absence of laser 2, taken over the course of around 30 seconds. A gaussian fit is applied to calculate the best guess estimate of $\Delta n^{I_0/2}$ along with the associated uncertainty.

The negative cross-Kerr nonlinearity could be due to the second fluid beam pumping atoms away from the ground state into the excited state, thus making the medium more transparent to the first fluid beam with less powerful interactions. The increase in cross-Kerr nonlinearity between the two negative dips is likely due to the second fluid beam approaching resonance, which in turn makes the medium opaque (to the second fluid beam) and significantly diminishes the optical path it traverses. Since the second fluid beam is absorbed rapidly within the cell, its contribution to the cross-Kerr nonlinearity diminishes.

The small increase of cross-Kerr nonlinearity could be explained by the second fluid beam pumping the medium's atoms into the ground state, thus increasing the opacity of the first fluid beam, and in turn increasing the strength of photon-photon interactions.

In the second case, the majority of the light intensity goes into the fluid beam issued from laser 2, such that $I_1 + I_2 \approx I_2 \approx I_0$, with $I_1 \ll I_2$. In this situation, measuring the nonlinear index of fluid beam 1 in the presence of both lasers directly gives the cross-Kerr nonlinearity, $\Delta n \approx n_{12}I_2$.

Figure 10 showcases the second method. The first fluid beam is set to around 50 mW, while the second fluid beam is set to around 350 mW. The results from this method seem to be dubious at best. For one, the measured nonlinearity, which is supposed to be entirely due to the cross-Kerr nonlinear index, is of the order of 10^{-5} , in direct contradiction with the first method. It is possible that this is due to the intensity of the first fluid beam not being low enough. Unfortunately lowering its intensity was not an option, because there were issues with the camera imaging being too faint or completely dark. Moreover, there is a frequency window at which the measured values of Δn are invalid, or present an unusually high uncertainty. This is again likely due to the second laser beam approaching resonance within the rubidium vapour cell, thus making the camera's image too faint for proper processing. These issues forbid making any physical interpretation of figure 10.

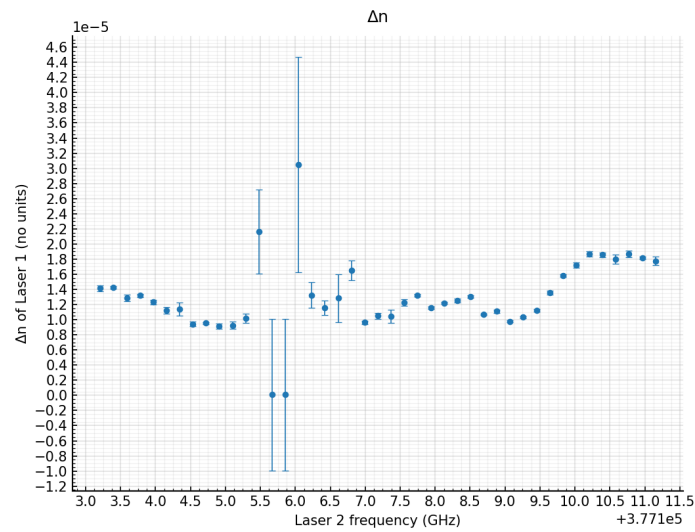


Figure 10: Plot showcasing the cross-Kerr nonlinear index of laser 1 (as explained in the second case of section 5) in function of the frequency of laser 2.

6 Conclusion

Quantum fluids of light provide a unique perspective to probe into the physics of quantum hydrodynamic systems, bringing with them their own advantages and challenges.

Although measuring the cross-Kerr interaction in itself takes a matter of a few seconds, creating an experimental setup, and developing the tools to measure it in a reliable and automated manner took much of the internship's time.

To my chagrin, the internship was short-lived, and much of the work put into it had to be cut prematurely. This is especially unfortunate since most of the measurements and data presented in this report were taken in the last few days of the internship. Thankfully, the work will be continued by S. Lepleux, and with a bit of luck, there will soon be more data to present (potentially at the oral examination of the internship).

In any case, this internship was a truly enriching experience that allowed me to dive into the deep end of physics research, and I must thank all of the QFL team for creating a welcoming and intellectually nourishing environment.

References

- [1] Glorieux, Q., Piekarski, C., Schibler, Q., Aladjidi, T. & Baker-Rasooli, M. Paraxial fluids of light (2025). URL <https://arxiv.org/abs/2504.06262>. 2504.06262.
- [2] Aladjidi, T. *Full optical control of quantum fluids of light in hot atomic vapors*. Theses, Sorbonne Université (2023). URL <https://theses.hal.science/tel-04391272>.
- [3] Piekarski, C., Cherroret, N., Aladjidi, T. & Glorieux, Q. Spin and density modes in a binary fluid of light (2025). URL <https://arxiv.org/abs/2412.08718>. 2412.08718.
- [4] Gliott, E., Piekarski, C. & Cherroret, N. Coarsening of binary bose superfluids: an effective theory (2025). URL <https://arxiv.org/abs/2504.12462>. 2504.12462.
- [5] Boyd, R. W. Chapter 1 - the nonlinear optical susceptibility. In Boyd, R. W. (ed.) *Nonlinear Optics (Third Edition)*, 1–67 (Academic Press, Burlington, 2008), third edition edn. URL <https://www.sciencedirect.com/science/article/pii/B9780123694706000010>.
- [6] Boyd, R. W. Chapter 2 - wave-equation description of nonlinear optical interactions. In Boyd, R. W. (ed.) *Nonlinear Optics (Third Edition)*, 69–133 (Academic Press, Burlington, 2008), third edition edn. URL <https://www.sciencedirect.com/science/article/pii/B9780123694706000022>.
- [7] Alcock, C. B., Itkin, V. P. & and, M. K. H. Vapour pressure equations for the metallic elements: 298–2500k. *Canadian Metallurgical Quarterly* **23**, 309–313 (1984). URL <https://doi.org/10.1179/cmq.1984.23.3.309>.
- [8] Van Stryland, E. W. & Sheik-Bahae, M. Z-scan technique for nonlinear materials characterization. In *Society of Photo-Optical Instrumentation Engineers (SPIE) Conference Series*, vol. 10291 of *Society of Photo-Optical Instrumentation Engineers (SPIE) Conference Series*, 102910Q (1997).
- [9] Boudebs, G., Chis, M. & Phu, X. N. Third-order susceptibility measurement by a new mach–zehnder interferometry technique. *J. Opt. Soc. Am. B* **18**, 623–627 (2001). URL <https://opg.optica.org/josab/abstract.cfm?URI=josab-18-5-623>.
- [10] Šantić, N. *et al.* Nonequilibrium precondensation of classical waves in two dimensions propagating through atomic vapors. *Phys. Rev. Lett.* **120**, 055301 (2018). URL <https://link.aps.org/doi/10.1103/PhysRevLett.120.055301>.

